On a three-dimensional Compton scattering tomography system with fixed source

J Cebeiro[1,*] , **C Tarpau**[2,3,4] , **M A Morvidone**[1] ,
D Rubio[1] **and M K Nguyen**[2]

[1] Centro de Matemática Aplicada, Universidad Nacional de San Martín (UNSAM),
Buenos Aires, Argentina
[2] Equipes Traitement de l'Information et Systèmes, CY Cergy Paris University,
ENSEA, CNRS UMR 8051, Cergy-Pontoise, France
[3] Laboratoire de Physique Théorique et Modélisation, CY Cergy Paris University,
CNRS UMR 8089, Cergy-Pontoise, France
[4] Laboratoire de Mathématiques de Versailles, Université de Versailles
Saint-Quentin, CNRS UMR 8100, Versailles, France

E-mail: jcebeiro@unsam.edu.ar

CrossMark

Abstract

Compton scattering tomography is an emerging scanning technique with attractive applications in several fields such as non-destructive testing and medical imaging. In this paper, we study a modality in three dimensions that employs a fixed source and a single detector moving on a spherical surface. We also study the Radon transform modeling the data that consists of integrals on toric surfaces. Using spherical harmonics we arrive to a generalized Abel's type equation connecting the coefficients of the expansion of the data with those of the function. We show the uniqueness of its solution and so the invertibility of the toric Radon transform. We illustrate this through numerical reconstructions in three dimensions using a regularized approach.

Keywords: Compton scatter imaging, 3D Compton tomography, Radon transforms, toric transform, spherical harmonic expansion of 3D discrete functions

(Some figures may appear in colour only in the online journal)

1. Introduction

Compton scattering imaging takes advantage of scattered radiation in order to explore the interior of an object under study. The basis of Compton scattering imaging is Compton effect

*Author to whom any correspondence should be addressed.

where a photon of energy E_0 interacts with an electron undergoing a change in its direction and losing part of its of energy. The angular deviation ω experienced by the photon and its remaining energy $E(\omega)$ are related by the well-known Compton formula

$$E(\omega) = \frac{E_0}{1 + \frac{E_0}{mc^2}(1 - \cos \omega)},$$

where E_0 is the energy of the incident photon and mc^2 is the energy of the electron at rest (511 keV). Transmission Compton scattering tomography consists in illuminating the object under study with a source of radiation and registering the scattered photons in its neighborhood. In this case the function to recover is a map of the electronic density of the object [1]. The interest in Compton scattering imaging is supported by its numerous potential applications namely non-destructive testing [2], airport security [3] and the study of composite materials, for instance those used in aircraft industry [4]. Recent works in medical imaging suggest potential advantages in diagnosis since images may exhibit better contrast in certain scenarios such as lung tumors [5, 6].

The first formulation of Compton tomography based on a Radon type transform has been introduced by Norton in [1]. The mathematical foundations arising from the seminal works of Cormack on circular Radon transforms provide a formal framework to study these modalities [7–9]. Depending on the setup, forward models are based on integral transforms on different manifolds. In a two-dimensional configuration, where collimated sources are used to restrict photons to a given scanning plane, manifolds are circular arcs [1, 2, 10–15]. If uncollimated detectors are used, manifolds consist in toric sections [3, 16, 17].

In three-dimensional Compton scattering tomography, where uncollimated source and detectors are employed, photons recorded at a given place and energy carry information about the electronic density all over a toric surface. In these setups scanning is performed in a volume rather than in a plane and the stacking of planar slices after reconstruction is no longer necessary. The problem in three dimensions has recently been addressed in [18] where a comprehensive framework was introduced together with four three-dimensional modalities. This framework takes attenuation into account and provides a back-projection algorithm for contour reconstruction. For some of these configurations, there are also results on injectivity, uniqueness and numerical reconstructions of the electronic density [3, 19].

The design of an operating Compton scattering tomography system raises numerous challenges involving size, detectors, sources, shielding and precise mechanisms to move components, sometimes in a synchronous fashion. In this respect, the suppression of the need of synchronized movements, the ability to scan a large object without surrounding it and the reduction of the number of moving components are advantageous design features. For instance, employing one fixed source turns valuable, particularly when using electrically powered sources that are expected to be more difficult to handle because of its weight and wiring. An extra difficulty in 3D CST is related to the algorithmic implementation. If the problem of reconstruction is addressed in the 3D Cartesian domain using matrix based methods, for instance iterative techniques, the large matrices involved can limit the resolution. Another challenge is connected to attenuation that can be modeled through weighed toric transforms.

Here, we study a Compton scattering tomography in three dimensions with one fixed central source and unique detector moving on a sphere. In particular, we show the invertibility of the toric transform modeling data acquisition. Instead of forcing the object under study to be strictly inside the detection sphere [18], we placed it strictly outside. Through this relative positioning of the specimen, the scanning can be carried out using a compact system without the need of enclosing or surrounding the object. This makes the configuration suitable for scanning large bodies or objects attached to major structures. Recently, a two-dimensional reduction of

this model has been studied in [17]. This reduction enabled to solve the reconstruction problem through an analytic reconstruction formula. Nevertheless, the setup requires translational relative movement between the object and the source in order to scan planar sections to be stacked in a three-dimensional reconstruction. There are 3D CST modalities for which object reconstruction has been shown feasible by means of the invertibility of its Radon transform. Two configurations, both registering back-scattered photons [3, 19], are suitable for scanning an object without surrounding it. While [19] requires the rotation of the pair source-detector, the design in [3] requires translational movement of the source that can be alternatively accomplished employing an array of multiple sources. Both modalities employ the same type of photons as ours (back-scattered). There is also a setup in [19] that employs forward-scattered photons to scan a body inside the sphere enclosed by the source-detector pair.

In order to model the forward problem, we formulate a Radon transform on tori and study its properties, particularly those connected to the uniqueness of its solution. The paper is organized as follows. In section 2 we explain briefly the setup, the scanning protocol and the toric Radon transform used to model image formation. We also write the transform as a spherical harmonics expansion and obtain an explicit Abel's type equation relating the coefficients of the expansion of the data with those of the function that represents the electronic density, i.e. the sought function. In section 3, we analyze its kernel and show the uniqueness of its solution proving, thus, the invertibility of the toric Radon transform. The approach we used to this end is different for those already used for studying other toric transforms and relies on the analysis of the gradient of the kernel. Numerical reconstructions based on discrete spherical harmonics and Tikhonov regularization are shown in section 4. This algorithm allows to reduce the 3D problem to a set of independent 1D problems limiting, thus, the size of the matrices involved. Reconstructions show that the scanning system can be smaller than the object. In section 5 we discuss some important issues such as the effect of neglecting attenuation and strategies to incorporate the influence of attenuation both in the theoretical analysis and reconstructions. Finally, we close the paper with some conclusions. Technical details of the spherical harmonics expansion, the analysis of the kernel and the algorithm we used in the discrete expansion are given in appendices A–C.

## 2. A setup for three-dimensional Compton scattering tomography

We introduce a setup for Compton scattering tomography based on a central source of radiation S located at the origin of coordinates. A single detector D moves at a constant distance R of the origin describing a sphere, as shown in figure 1. The property to recover is the electronic density $f(x, y, z)$ of an object placed strictly outside of this spherical surface. Detector D registers backscattered photons of energy $E(\omega)$ that have interacted with electrons of the object and deviated an angle ω from its original path. When detector D is at position labeled by angles (α, β) and registers a photon of energy $E(\omega)$, the interaction site is located somewhere on the surface of an apple torus through points S and D, which is characterized by α, β and ω. Thus, the flux of photons of energy $E(\omega)$ registered by D at sites (α, β) is proportional to the integral of function f on a toric surface $\mathcal{T}^{\omega, \alpha, \beta}$, with $\alpha \in [0, 2\pi)$, $\beta \in [0, \pi]$ and $\omega \in (\pi/2, \pi)$, see figures 1 and 2. Notice that the referred torus may be generated by the rotation of a toric section around segment $\overline{SD}$, see figure 2.

Before giving the definition of the Radon transform modeling the forward problem, let us introduce some notation. The coordinates of the detector D are given by

$$D(\alpha, \beta) = R(\cos \alpha \, \sin \beta, \sin \alpha \, \sin \beta, \cos \beta)^T, \quad \alpha \in [0, 2\pi), \ \beta \in [0, \pi].$$
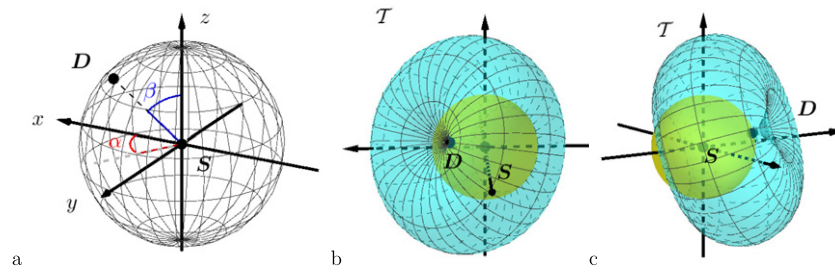
Figure 1. (a) Setup of the new CST modality: source (S), detector (D), detection sphere (mesh). (b) and (c) Two views of an apple torus $\mathcal{T}$ (blue) and the detection sphere (yellow).
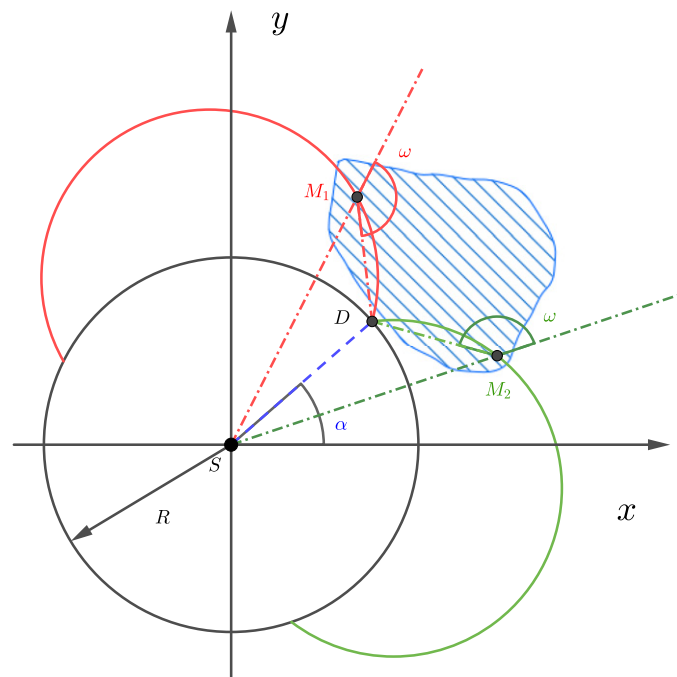
Figure 2. Planar section ($z = 0$) of the setup and the manifold. Toric section (continuous curves red and green) rotates around $\overline{SD}$ to generate the torus. S: source, D: detector, ω: scattering angle, M_1 and M_2: scattering sites, R: radius of the detection sphere. In this case, the detector is placed at angles $\alpha < \pi/2$ and $\beta = \pi/2$.

We define a parametrization of any torus $\mathcal{T}^{\omega,\alpha,\beta}$ as:

$$\Phi^{\omega,\alpha,\beta}(\gamma, \psi) = r^{\omega}(\gamma)\Theta^{\alpha,\beta}(\gamma, \psi), \tag{1}$$

with $\gamma \in (0, 2\omega - \pi)$, $\psi \in (0, 2\pi)$. Here, the radial part is given by

$$r^{\omega}(\gamma) = R\frac{\sin(\omega - \gamma)}{\sin \omega},$$

while the angular part is expressed as $\Theta^{\alpha,\beta}(\gamma,\psi) = u(\alpha)a(\beta)\Theta(\gamma,\psi)$, where

$$\Theta(\gamma,\psi) = (\cos\psi\ \sin\gamma, \sin\psi\ \sin\gamma, \cos\gamma)^T,$$

is a point on S^2, the unit sphere in $\mathbb{R}^3$, and

$$u(\alpha) = \begin{pmatrix} \cos\alpha & -\sin\alpha & 0 \\ \sin\alpha & \cos\alpha & 0 \\ 0 & 0 & 1 \end{pmatrix}\ \text{and}$$

$$a(\beta) = \begin{pmatrix} \cos\beta & 0 & \sin\beta \\ 0 & 1 & 0 \\ -\sin\beta & 0 & \cos\beta \end{pmatrix}, \tag{2}$$

are a rotation of angle α about the z-axis and a rotation of angle β about the y-axis, respectively. Finally, given positive numbers r_M, r_m such that $r_M > r_m > R > 0$, we define the spherical shell $S_h(r_m, r_M)$ as

$$S_h(r_m, r_M) = \{(x,y,z) \in \mathbb{R}^3 : r_m \leqslant \sqrt{x^2 + y^2 + z^2} \leqslant r_M\}.$$

We are now ready to introduce the toric Radon transform associated to this modality.

Definition. Let $f(x,y,z)$ be a compact supported function with support contained in $S_h(r_m, r_M)$. We define the toric Radon transform $\mathcal{R}_{\mathcal{T}}f$ of function f as $\mathcal{R}_{\mathcal{T}}f(\alpha,\beta,\omega) = \int_{T^{\omega,\alpha,\beta}} \mathrm{d}S_{\mathcal{T}}f(x,y,z)$. Explicitly

$$\mathcal{R}_{\mathcal{T}}f(\alpha,\beta,\omega) = \int_0^{2\omega-\pi} \mathrm{d}\gamma \int_0^{2\pi} \mathrm{d}\psi\, f\left(\Phi^{\omega,\alpha,\beta}(\gamma,\psi)\right) r^{\omega}(\gamma)\frac{\sin\gamma}{\sin\omega}, \tag{3}$$

where $\omega \in (\frac{\pi}{2}, \pi)$, $\alpha \in [0, 2\pi)$, $\beta \in [0, \pi]$.

Equation (3) is the forward operator that models the data recorded, this integral transform is rotational invariant. Its manifold is the part of an apple torus through the origin outside of the sphere of radius R. In [19], the authors studied another rotational invariant toric transform whose manifold was an apple torus that did not pass through the origin. Interesting issues on the toric Radon transform (3) such as spherical harmonics expansion [20], rotational invariance and invertibility [21] can be studied, in what follows we address some of them.

2.1. Spherical harmonics expansion

In this section, we explicit the connection between the components of the spherical harmonics expansion of a function f and those of its toric Radon transform $\mathcal{R}_{\mathcal{T}}f$. Spherical harmonics of degree l and order m are defined as:

$$Y_l^m(\gamma,\psi) = (-1)^m \sqrt{\frac{(2l+1)(l-m)!}{4\pi(l+m)!}} P_l^m(\cos\gamma)\mathrm{e}^{\mathrm{i}m\psi}, \tag{4}$$

where $\gamma \in [0,\pi]$, $\psi \in [0, 2\pi)$ and $P_l^m(x)$ is the Legendre polynomial of degree l and order m, see [20, 22] for details. The set $\{Y_l^m\}$, for $l \in \mathbb{N}$ and $|m| \leqslant l$ is a complete orthonormal system in S^2. Any function $f \in C^{\infty}(\mathbb{R}^3)$ can be expanded in terms of $Y_l^m(\gamma,\psi)$ according to

$$f(r\Theta(\gamma,\psi)) = \sum_{l=0}^{\infty} \sum_{|m| \leqslant l} f_{lm}(r) Y_l^m(\gamma,\psi), \tag{5}$$

where

$$f_{lm}(r) = \langle f, Y_l^m \rangle = \int_0^{2\pi} \int_0^\pi f(r\Theta(\gamma, \psi)) \overline{Y_l^m(\gamma, \psi)} \sin \gamma \, d\gamma \, d\psi,$$

and $\langle , \rangle$ is the scalar product in $L^2(S^2)$, the overline denotes complex conjugation, and $r \in \mathbb{R}_0^+$ is fixed.

Following the ideas in [19], it can be shown that the spherical harmonics expansion of $\mathcal{R}_\mathcal{T} f$ can be written as

$$\mathcal{R}_\mathcal{T} f(\alpha, \beta, \omega) = \sum_{l \in \mathbb{N}} \sum_{|m| \leqslant l} (\mathcal{R}_\mathcal{T} f)_{lm}(\omega) Y_l^m(\alpha, \beta), \tag{6}$$

where coefficients in the expansion are given by the following lemma, see appendix A for a proof.

Lemma 2.1. *The Fourier coefficients of data $(\mathcal{R}_\mathcal{T} f)_{lm}$ in (6) and those of the object f_{lm} are related by*

$$(\mathcal{R}_\mathcal{T} f)_{lm}(\omega) = 2\pi \int_0^{2\omega - \pi} d\gamma \, r^\omega(\gamma) \frac{\sin \gamma}{\sin \omega} f_{lm}(r^\omega(\gamma)) P_l^0(\cos \gamma), \tag{7}$$

where $P_l^0(.)$ is the zero order associated Legendre polynomial of degree l.

3. Uniqueness of the solution of the toric Radon transform

We address now the question of the uniqueness of solutions of (3) using spherical harmonics expansions. In section 3.1 we show that (7) is a generalized Abel type integral equation with a kernel with zeros on its diagonal. In section 3.2 we analyze the properties of the kernel to prove invertibility.

3.1. An alternative expression for the integral equation

We split up (7) in two parts having integration range $(0, \omega - \frac{\pi}{2})$ and $(\omega - \frac{\pi}{2}, 2\omega - \pi)$, respectively and perform the substitution $\gamma = \omega - \sin^{-1}\left(\frac{r \sin \omega}{R}\right)$ in the first integral and $\gamma = \omega + \sin^{-1}\left(\frac{r \sin \omega}{R}\right) - \pi$ in the second one. After some calculations, making use of the identities $\cos(\sin^{-1}) = \sqrt{1 - x^2}$ and $P_l^0(-x) = (-1)^l P_l^0(x)$ (see, for example, [23]), we arrive to

$$(\mathcal{R}_\mathcal{T} f)_{lm}(\omega) = \int_R^{\frac{R}{\sin \omega}} dr \, f_{lm}(r) \frac{1}{\sqrt{\left(\frac{R}{\sin \omega}\right) - r}}$$

$$\times \frac{2\pi}{\sin \omega} \sum_{\sigma = \pm 1} \frac{r \sin\left(\sin^{-1}\left(\frac{r \sin \omega}{R}\right) - \sigma\omega\right)}{\sqrt{\left(\frac{R}{\sin \omega}\right) + r}} (\sigma)^l$$

$$\times P_l^0 \left(\cos\left(\omega - \sigma \sin^{-1}\left(\frac{r \sin \omega}{R}\right)\right) \right). \tag{8}$$

The support of function $f_{lm}(r)$ enables to replace the lower integration limit R by r_m. Making the substitution $p = R/\sin\omega$[5] and keeping the notation for readability[6], the integral equation reads:

$$(\mathcal{R}_\mathcal{T} f)_{lm}(p) = \int_{r_m}^p \mathrm{d} r \, f_{lm}(r) \, \frac{1}{\sqrt{p-r}} K_l(p, r), \tag{9}$$

where the kernel is

$$K_l(p, r) = \frac{2\pi}{R} \sum_{\sigma=\pm1} \sigma^l \frac{pr \, \sin\left(\sin^{-1}\left(\frac{r}{p}\right) - \sigma \sin^{-1}\left(\frac{R}{p}\right)\right)}{\sqrt{p+r}}$$

$$\times P_l^0\left(\cos\left(\sin^{-1}\left(\frac{R}{p}\right) - \sigma \sin^{-1}\left(\frac{r}{p}\right)\right)\right). \tag{10}$$

Now, we rewrite kernel (10) in a suitable form for the evaluation of the existence of a unique solution of (7). Using elementary geometry, we can express the kernel as

$$K_l(p, r) = \sum_{\sigma=\pm1} \left(Q_1 - \sigma Q_2 \sqrt{p-r}\right) \sigma^l P_l^0 \left(Q_3 \sqrt{p-r} + \sigma Q_4\right), \tag{11}$$

where

$$Q_1 = Q_1(p, r) = \frac{2\pi r^2 \sqrt{p^2 - R^2}}{Rp\sqrt{p+r}}, \tag{12}$$

$$Q_2 = Q_2(p, r) = \frac{2\pi r}{p}, \tag{13}$$

$$Q_3 = Q_3(p, r) = \frac{\sqrt{p^2 - R^2}\sqrt{p+r}}{p^2}, \tag{14}$$

$$Q_4 = Q_4(p, r) = \frac{Rr}{p^2}. \tag{15}$$

Using the binomial formula to expand each term of $P_l^0(x) = a_l x^l + \cdots + a_1 x + a_0$, with $x = Q_3\sqrt{p-r} + \sigma Q_4$, we have

$$\begin{aligned}
K_l(p, r) &= \sum_{\sigma=\pm1} \left(Q_1 - \sigma Q_2 \sqrt{p-r}\right) \sigma^l P_l^0 \left(Q_3 \sqrt{p-r} + \sigma Q_4\right) \\
&= \left(Q_1 + Q_2 \sqrt{p-r}\right) (-1)^l P_l^0 \left(Q_3 \sqrt{p-r} - Q_4\right) \\
&\quad + \left(Q_1 - Q_2 \sqrt{p-r}\right) P_l^0 \left(Q_3 \sqrt{p-r} + Q_4\right) \\
&= \left(Q_1 + Q_2 \sqrt{p-r}\right) \sum_{n=0}^l a_n \left(-Q_3 \sqrt{p-r} + Q_4\right)^n
\end{aligned}$$

---

[5] Physically p is the diameter of the circles that generate the torus as a surface of revolution.

[6] Strictly speaking, we should have changed the function after this substitution, for instance $(\mathcal{R}_\mathcal{T} f)_{lm}(\sin^{-1} R/p) = \left(\widetilde{\mathcal{R}_\mathcal{T} f}\right)_{lm}(p)$.

$$+ \left(Q_1 - Q_2\sqrt{p-r}\right) \sum_{n=0}^{l} a_n \left(Q_3\sqrt{p-r} + Q_4\right)^n$$

$$= \left(Q_1 + Q_2\sqrt{p-r}\right) \sum_{n=0}^{l} a_n \sum_{k=0}^{n} \binom{n}{k} \left(-Q_3\sqrt{p-r}\right)^{n-k} Q_4^k$$

$$+ \left(Q_1 - Q_2\sqrt{p-r}\right) \sum_{n=0}^{l} a_n \sum_{k=0}^{n} \binom{n}{k} \left(Q_3\sqrt{p-r}\right)^{n-k} Q_4^k.$$

Finally, we get to

$$K_l(p,r) = \sum_{n=0}^{l} a_n \sum_{k=0}^{n} \binom{n}{k} Q_3^{n-k} Q_4^k \left[\left((-1)^{n-k} + 1\right) Q_1 \sqrt{p-r}^{\,n-k} \right.$$

$$\left. + \left((-1)^{n-k} - 1\right) Q_2 \sqrt{p-r}^{\,n-k+1} \right]. \tag{16}$$

After performing some calculations (see appendix B) we arrive to

$$K_l(p,r) = 2Q_1 \sum_{n=0}^{l} a_n Q_4^n + 2(p-r) \left[\frac{1}{2} Q_3^2 Q_1 \sum_{n=2}^{l} a_n n(n-1) Q_4^{n-2} \right.$$

$$\left. - Q_3 Q_2 \sum_{n=1}^{l} a_n n Q_4^{n-1} \right]$$

$$+ \sum_{n=3}^{l} a_n \sum_{k=0}^{n-3} \binom{n}{k} Q_3^{n-k} Q_4^k \left[\left((-1)^{n-k} + 1\right) Q_1 \sqrt{p-r}^{\,n-k} \right.$$

$$\left. + \left((-1)^{n-k} - 1\right) Q_2 \sqrt{p-r}^{\,n-k+1} \right]. \tag{17}$$

Notice that summations on the first line correspond to Legendre polynomials and their first and second order derivatives evaluated in Q_4. In the second line, terms with odd powers of $\sqrt{p-r}$ vanish and only powers of $(p-r)$ greater than or equal to 2 remain. Then, using a compact notation for Legendre polynomials $P(.) = P_l^0(.)$ and its derivatives $P'(.)$ and $P''(.)$, and splitting up summations in order to define a new subindex, we have

$$K_l(p,r) = 2Q_1 P(Q_4) + 2(p-r) \left[\frac{1}{2} Q_3^2 Q_1 P''(Q_4) - Q_3 Q_2 P'(Q_4) \right]$$

$$+ 2 \sum_{n=3}^{l} a_n \left[Q_1 \sum_{i=2}^{\lfloor \frac{n}{2} \rfloor} \binom{n}{n-2i} Q_3^{2i} Q_4^{n-2i} (p-r)^i - Q_2 \right.$$

$$\left. \times \sum_{i=2}^{\lfloor \frac{n+1}{2} \rfloor} \binom{n}{n-2i+1} Q_3^{2i-1} Q_4^{n-2i+1} (p-r)^i \right]. \tag{18}$$

Equation (18) is useful for studying the properties of the kernel in order to prove invertibility. Particularly, (18) is more suitable for differentiation on the diagonal $p = r$ according theorem 3.1 in next section.

3.2. On the invertibility of $\mathcal{R}_\mathcal{T}f$ in terms of spherical harmonics

Equation (9) is a generalized Abel type equation. Notice that kernel (18) has zeros on the diagonal $p = r$, since the Legendre polynomials have zeros in the interval $[0, 1]$. Recently, Schiefeneder and Haltmeier stated conditions for the uniqueness of the solution of this kind of equations with kernels with zeros on its diagonal [24]. For the sake of completeness, we present their results in the following lemma.

Lemma 3.1 ([24], theorem 3.4).   *Consider the generalized Abel type integral equation*

$$\forall t \in [a, b] : g(t) = \int_a^t \mathrm{d}s\, f(s) \frac{1}{\sqrt{t - s}} K(t, s), \tag{19}$$

where $g \in C([a, b])$ and $K \in C(\Delta(a, b))$, with $\Delta(a, b) := \{a \leqslant s \leqslant t \leqslant b\}$, is a continuous kernel having zeros on the diagonal. Suppose $K : \Delta(a, b) \to \mathbb{R}$, where $a < b$, satisfies the following assumptions:

(a) $K \in C^3(\Delta(a, b))$.
(b) $N_K := \{s \in [a, b] | K(s, s) = 0\}$ *is finite and consists of simple roots.*
(c) *For every $s \in N_K$, the gradient $(\kappa_1, \kappa_2) = \nabla K(s, s)$ satisfies*

$$1 + \frac{1}{2} \frac{\kappa_1}{\kappa_1 + \kappa_2} > 0.$$

Then, for any $g \in C([a, b])$, equation (19) has at most one solution $f \in C([a, b])$.

We are now ready to introduce our claim.

Theorem 3.1 (Invertibility of equation (9)).   For   any $(\mathcal{R}_\mathcal{T}f)_{lm} \in C([r_m, r_M])$, *equation (9) has at most one solution $f_{lm} \in C([r_m, r_M])$.*

Proof.   In order to show the uniqueness of the solution of (9), we use lemma 3.1. So, we must check assumptions (a), (b) and (c). We define the triangle $\triangle(r_m, r_M) := \{r_m \leqslant r \leqslant p \leqslant r_M\}$.

(a) As it is evident from (11), the kernel is smooth inside $\Delta(r_m, r_M)$. Notice in (16) that terms containing odd powers of $\sqrt{p - r}$ always vanish. Moreover, the double summation involves only non-negative integer powers of $p - r$ times products of powers of factors Q_1, Q_2, Q_3 and Q_4. Since all the functions involved are smooth on the diagonal $p = r$, so is K_l.

(b) From (18) we obtain the expression for the kernel on the diagonal

$$K_l(r, r) = \frac{\sqrt{8}\pi}{R} \sqrt{r} \sqrt{r^2 - R^2} P\left(\frac{R}{r}\right).$$

So, $K_l(r, r)$ has the same zeros as $P\left(\frac{R}{r}\right)$ since $0 < R < r_m \leqslant r$. Given that P is an orthogonal polynomial, $P\left(\frac{R}{r}\right)$ has a finite number of simple roots. Then, the values r_0 such that $P\left(\frac{R}{r_0}\right) = 0$ are the zeros of the kernel on the diagonal, i.e. $K_l(r_0, r_0) = 0$.

(c) We obtain an expression for $\nabla K_l(r, r)$ and evaluate it at zeros r_0. We see in (18) that the derivatives of terms containing factors $(p - r)^i$ with $i = 2, 3, \ldots$ vanish on the diagonal $p = r$. So, we define a new function

$$\overline{K}_l(p, r) = 2Q_1 P(Q_4) + 2(p - r) \left[\frac{1}{2} Q_3^2 Q_1 P''(Q_4) - Q_3 Q_2 P'(Q_4) \right], \tag{20}$$

which verifies $\nabla K_l(r, r) = \nabla \overline{K}_l(r, r)$ and is easier to handle. Then, we differentiate $\overline{K}_l$ with respect to p

$$\frac{\partial \overline{K}_l}{\partial p}(p, r) = 2 \frac{\partial Q_1}{\partial p} P(Q_4) + 2Q_1 \frac{\partial}{\partial p} P(Q_4)$$

$$+ 2 \left[\frac{1}{2} Q_3^2 Q_1 P''(Q_4) - Q_3 Q_2 P'(Q_4) \right]$$

$$+ 2(p - r) \frac{\partial}{\partial p} \left[\frac{1}{2} Q_3^2 Q_1 P''(Q_4) - Q_3 Q_2 P'(Q_4) \right]. \qquad (21)$$

Using the identity $P''(x) = [2xP'(x) - l(l + 1)P(x)]/(1 - x^2)$, see for example [23, 25], and the fact that $Q_4(p, r) < 1$, we substitute $P''(Q_4)$ in the third term in (21), and we arrive to

$$\frac{\partial \overline{K}_l}{\partial p}(p, r) = \left(2 \frac{\partial Q_1}{\partial p} - \frac{Q_3^2 Q_1 l(l + 1)}{1 - Q_4^2} \right) P(Q_4)$$

$$+ 2(p - r) \frac{\partial}{\partial p} \left[\frac{1}{2} Q_3^2 Q_1 P''(Q_4) - Q_3 Q_2 P'(Q_4) \right]$$

$$+ 2 \left[Q_1 \frac{\partial Q_4}{\partial p} - Q_3 Q_2 + \frac{Q_3^2 Q_1 Q_4}{1 - Q_4^2} \right] P'(Q_4). \qquad (22)$$

We proceed identically for the other variable r

$$\frac{\partial \overline{K}_l}{\partial r}(p, r) = 2 \frac{\partial Q_1}{\partial r} P(Q_4) + 2Q_1 \frac{\partial}{\partial r} P(Q_4)$$

$$- 2 \left[Q_3^2 Q_1 \frac{1}{2} P''(Q_4) - Q_3 Q_2 P'(Q_4) \right]$$

$$+ 2(p - r) \frac{\partial}{\partial r} \left[\frac{1}{2} Q_3^2 Q_1 P''(Q_4) - Q_3 Q_2 P'(Q_4) \right] \qquad (23)$$

and we obtain

$$\frac{\partial \overline{K}_l}{\partial r}(p, r) = \left(2 \frac{\partial Q_1}{\partial r} + \frac{Q_3^2 Q_1 l(l + 1)}{1 - Q_4^2} \right) P(Q_4)$$

$$+ 2(p - r) \frac{\partial}{\partial r} \left[\frac{1}{2} Q_3^2 Q_1 P''(Q_4) - Q_3 Q_2 P'(Q_4) \right]$$

$$+ 2 \left[Q_1 \frac{\partial Q_4}{\partial r} + Q_3 Q_2 - \frac{Q_3^2 Q_1 Q_4}{1 - Q_4^2} \right] P'(Q_4). \qquad (24)$$

The explicit forms (22) and (24) simplify the calculation of $\frac{\partial K_l}{\partial r}(r, r)$ and $\frac{\partial K_l}{\partial p}(r, r)$. Evaluating at $p = r = r_0$, the first and second terms in (22) and (24) vanish. In fact, the first terms vanish because $P(Q_4(r_0, r_0)) = P(\frac{Rr_0}{r_0^2}) = P(\frac{R}{r_0}) = 0$, while the second terms vanish

because of the factor $(p - r)$. Thus, we have

$$(\kappa_1, \kappa_2) = \nabla K_l(r_0, r_0) = \nabla \overline{K}_l(r_0, r_0) = 2 \left(\left[Q_1 \frac{\partial Q_4}{\partial p} - Q_3 Q_2 + \frac{Q_3^2 Q_1 Q_4}{1 - Q_4^2} \right], \right.$$

$$\left. \left[Q_1 \frac{\partial Q_4}{\partial r} + Q_3 Q_2 - \frac{Q_3^2 Q_1 Q_4}{1 - Q_4^2} \right] \right) P'(Q_4) \bigg|_{p = r = r_0} . \tag{25}$$

We evaluate (25) using the definition of functions Q_1, Q_2, Q_3 and Q_4, then the expressions for the gradient components are

$$\kappa_1 = -4\pi P' \left(\frac{R}{r_0} \right) \frac{\sqrt{2r_0} \sqrt{r_0^2 - R^2}}{r_0^2}, \tag{26}$$

and

$$\kappa_2 = 2\pi P' \left(\frac{R}{r_0} \right) \frac{\sqrt{2r_0} \sqrt{r_0^2 - R^2}}{r_0^2}. \tag{27}$$

Finally, we get the ratio

$$1 + \frac{1}{2} \frac{\kappa_1}{\kappa_1 + \kappa_2} = 2 > 0,$$

as we wanted to show.

Thus, the radial components $f_{lm}(r)$ of function f can be recovered uniquely from the coefficients $(\mathcal{R}_{\mathcal{T}} f)_{lm}(p)$. ☐

We can express data in terms of variable p instead of the scattering angle ω

$$\mathcal{R}_{\mathcal{T}} f(p, \alpha, \beta) = \sum_{l \in \mathbb{N}} \sum_{|m| \leqslant l} (\mathcal{R}_{\mathcal{T}} f)_{lm}(p) Y_l^m(\beta, \alpha).$$

From the geometrical point of view, p is the diameter of the circles generating the torus, see section 4.1 for the integral definition of $\mathcal{R}_{\mathcal{T}} f(p, \alpha, \beta)$. The following corollary summarizes our result on uniqueness.

Corollary 3.1 (Invertibility of the $\mathcal{R}_{\mathcal{T}} f$). *If f_1 and f_2 are compact supported functions in $C^\infty(S_h(r_m, r_M))$ and $\mathcal{R}_{\mathcal{T}} f_1 = \mathcal{R}_{\mathcal{T}} f_2$, then $f_1 = f_2$.*

Proof. Let f satisfy $(\mathcal{R}_{\mathcal{T}} f)_{lm} = 0$ for all l, m in the spherical harmonics expansion. According to theorem 3.1, there is a unique solution $f_{lm} = 0$, which implies $f = 0$. The linearity of $\mathcal{R}_{\mathcal{T}} f$ yields the claim. ☐

4. Numerical simulations

We use a discrete spherical harmonics expansion of the functions representing the data and the object in order to carry out numerical reconstructions. We employ a product integration approach to model the discrete problem in the spherical harmonic domain. Then, Tikhonov regularization is used to solve a set of normal equations.

4.1. Alternative forward model

An alternative definition of our toric Radon transform useful in numerical simulation is

$$
\mathcal{R}_{\mathcal{T}} f(p, \alpha, \beta) = p^2 \int_0^\pi \mathrm{d}\gamma \int_0^{2\pi} \mathrm{d}\psi \, \cos\left(\gamma - \cos^{-1}\frac{R}{p}\right) \sin\gamma f\left(\Phi^{p,\alpha,\beta}(\gamma,\psi)\right),
\tag{28}
$$

where $p \in (R, +\infty)$ is the diameter of the circles making the torus and

$$
\Phi^{p,\alpha,\beta}(\gamma,\psi) = r\Theta^{\alpha,\beta}(\gamma,\psi)\big|_{r=p\,\cos\left(\gamma-\cos^{-1}\frac{R}{p}\right)},
\tag{29}
$$

is the parametrization of the toric surface labeled by variables (p, α, β). The unit vector $\Theta^{\alpha,\beta}(\gamma,\psi)$ was introduced in the definition (1). The scattering angle ω and the diameter p are related through $p = R/\sin\omega$.

4.2. The algebraic problem

In this section we use a discrete spherical harmonics expansion of order N to write the problem as an algebraic product suitable for Tikhonov regularization. This is achieved using numerical algorithms for the discrete-inverse spherical harmonics transform (DSHT-IDSHT), see an outline in appendix C, with data as well as with the sought function according to equations (30) and (31). The pair DSHT-IDSHT allows us to write the problem in the domain of the spherical harmonics according to

$$
\mathbf{g}_{nk}^j \underset{\text{IDSHT}}{\overset{\text{DSHT}}{\rightleftarrows}} \mathbf{g}_{lm}^j,
\tag{30}
$$

$$
\mathbf{f}_{nk}^i \underset{\text{IDSHT}}{\overset{\text{DSHT}}{\rightleftarrows}} \mathbf{f}_{lm}^i,
\tag{31}
$$

where the discrete functions are $\mathbf{g}_{nk}^j = \mathcal{R}_{\mathcal{T}}f(p_j, \alpha_n, \beta_k)$, $\mathbf{g}_{lm}^j = (\mathcal{R}_{\mathcal{T}}f)_{lm}(p_j)$ with $j = 0, \ldots, N_p - 1$, $\mathbf{f}_{nk}^i = f(r_i \cos\psi_n \sin\gamma_k, r_i \sin\psi_n \sin\gamma_k, r_i \cos\gamma_k)$ and $\mathbf{f}_{lm}^i = f_{lm}(r_i)$ with $i = 0, \ldots, N_r - 1$. Variables p and r are in the range $(R, r_M^*]$ where r_M^* is such that $r_M^* \geqslant r_M$ to cover the radial support of function f. In this domain, the components of the vector representing the unknown function $\mathbf{f}_{lm}$ are related to components of the vector for the known data $\mathbf{g}_{lm}$ through the equation $\mathbf{g}_{lm} = A_l \mathbf{f}_{lm}$ that is an algebraic relative of equation (9). We are aimed to solve the equation for each combination l, m.

4.3. Matrix generation

Matrix $A_l \in \mathbb{R}^{N_p \times N_r}$ is the key for solving the numerical inverse problem. Given that we use an expansion of order N and the kernel in (9) is l-dependent and m-independent, there are only $N + 1$ different matrices. Adopting the convention $Np = Nr = M$ and splitting up the integration range in equation (9), we rewrite

$$
(\mathcal{R}_{\mathcal{T}}f)_{lm}(p_j) = \sum_{q=1}^j \int_{r_{q-1}}^{r_q} \mathrm{d}r \, f_{lm}(r) \frac{r}{\sqrt{p_j^2 - r^2}} \tilde{K}_l(p_j, r),
\tag{32}
$$

Table 1. Sketch of the reconstruction algorithm.

Matrix A_l is precalculated according to (35)
1: Chose a suitable value for λ according to signal conditions
2: Perform DSHT (30) to data $\mathbf{g}_{nk}^j$ to obtain $\mathbf{g}_{lm}^j$
3: For each pair l, m: solve the normal equations in (36) and obtain an approximation of $\mathbf{f}_{lm}^i$
4: Perform IDSHT (31) to obtain the reconstruction $\mathbf{f}_{nk}^i$
5: Interpolate to obtain the function in discrete Cartesian coordinates $\tilde{\mathbf{f}}$

where $r_q = R + q(r_M^* - R)/M$ and $\tilde{K}_l(p_j, r) = \sqrt{p_j + r}K_l(p_j, r)/r$. We use product integration [26] but instead of using the mid-point rule we approximate $\tilde{K}_l(p_j, r)$ by its average $\tilde{K}_{l\,q}(p_j)$ in ten equidistant points in the interval $[r_{q-1}, r_q]$. Thus, the discrete form for the equation is

$$\mathbf{g}_{lm}^j = (\mathcal{R}_\mathcal{T} f)_{lm}(p_j) \simeq \sum_{q=1}^{j} w_{j,q} \tilde{K}_{l\,q}(p_j) f_{lm}(r_q), \tag{33}$$

where the weighting factor has been calculated analytically according to

$$w_{j,q} := \int_{r_{q-1}}^{r_q} \mathrm{d}r \frac{r}{\sqrt{p_j^2 - r^2}}, \tag{34}$$

with $j, q = 1, \ldots, M$ and $w_{j,q} = 0$ if $j < q$. Finally, the entries of the lower-triangular matrix in equation $\mathbf{g}_{lm} = A_l \mathbf{f}_{lm}$ are

$$A_l = \left(w_{j,q} \tilde{K}_{l\,q}(p_j) \right)_{j,q=1,\ldots M} \in \mathbb{R}^{M \times M}. \tag{35}$$

4.4. Overview of the reconstruction algorithm

The aim now is recovering vector $\mathbf{f}_{lm}$ from $\mathbf{g}_{lm}$ using the equation $\mathbf{g}_{lm} = A_l \mathbf{f}_{lm}$. When A_l is non-singular and well-conditioned the problem can be easily solved by forward substitution. Because the kernel has zeros on its diagonal, matrix A_l may have diagonal entries being zero or close to zero. Thus, solving the system may be ill-conditioned and regularization methods must be applied. The algorithm is summarized in table 1 and is aimed to solve the matrix problem $\mathbf{g}_{lm} = A_l \mathbf{f}_{lm}$ for $l = 0, \ldots, N$ and $|m| \leqslant l$. Tikhonov regularization requires to solve the normal equations

$$(A_l^T A_l + \lambda I)\mathbf{f}_{lm} = A_l^T \mathbf{g}_{lm}, \tag{36}$$

where I is the identity matrix and λ is a regularization parameter.

For non-vanishing kernel diagonals, the product integration method is convergent [27]. To the best of our knowledge, there are no reported results on the convergence of product integration with vanishing kernel-diagonals. As suggested in [26], numerical evidence indicate that, for a suitable selection of the regularization parameter, a convergence analysis may be possible.

4.5. Results

Data was simulated using equation (28), a system where detector moves on a sphere of radius $R = 1/8$ was considered. The object was a $64 \times 64 \times 64$ volume with two balls with different intensities, and different contrasts, gray on black, white on gray, etc. One object has also a
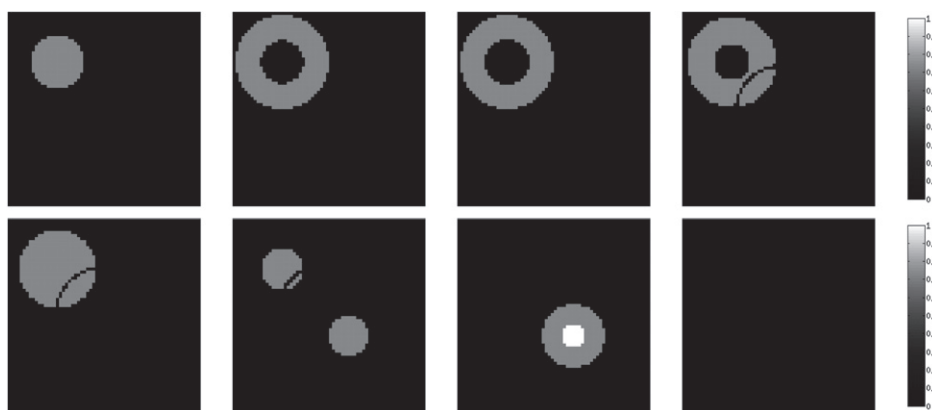
Figure 3. Original 3D phantom used for simulations. Notice the crack in some planes.
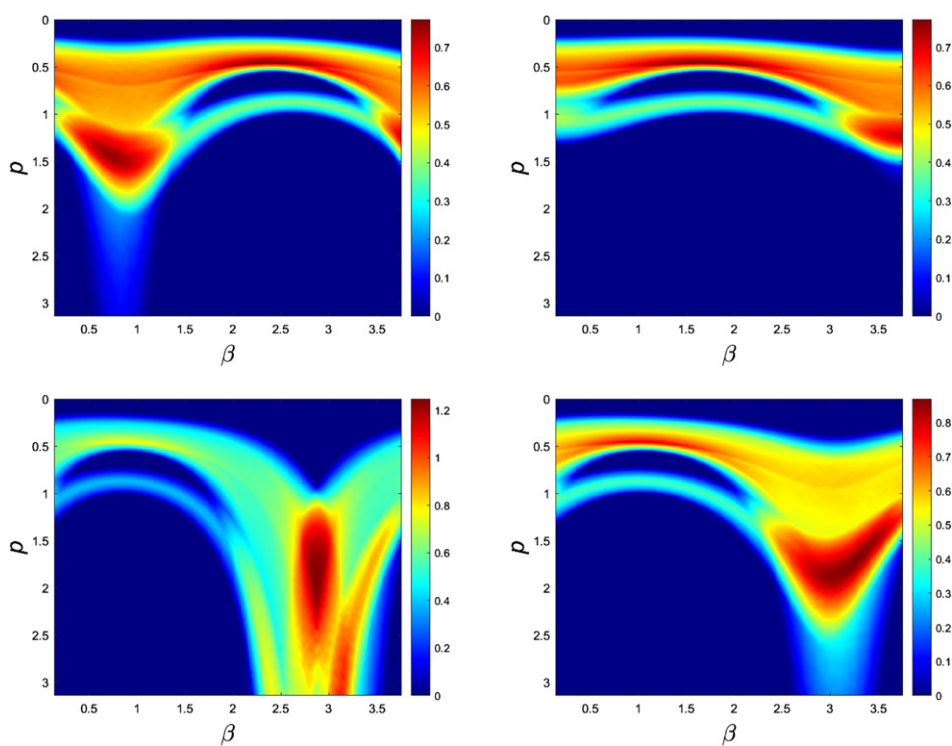

Figure 4. Data simulated using (28). Function $\mathcal{R}_{\mathcal{T}}(p, \alpha, \beta)$ is shown for the sets $\alpha = 0, 3\pi/4, 5\pi/4, 3\pi/2$.

defect (crack) in some planes, see figure 3. The function was supported in a cube of side $L = 1$ in the first octant with coordinate $(x_{\min}, y_{\min}, z_{\min}) = (L/64, L/64, R)$. Discretization parameters of data are: $N_\alpha = 513$, $N_\beta = 256$ and $N_p = 512$. The maximal diameter of the circles generating the torus is $r_M^* = 2r_M$ where $[R, r_M^*]$ is the radial support of the cube containing the phantom. Numerical integration is performed in variables γ and ψ with $\Delta\psi = 2\pi/N_\psi$ and the
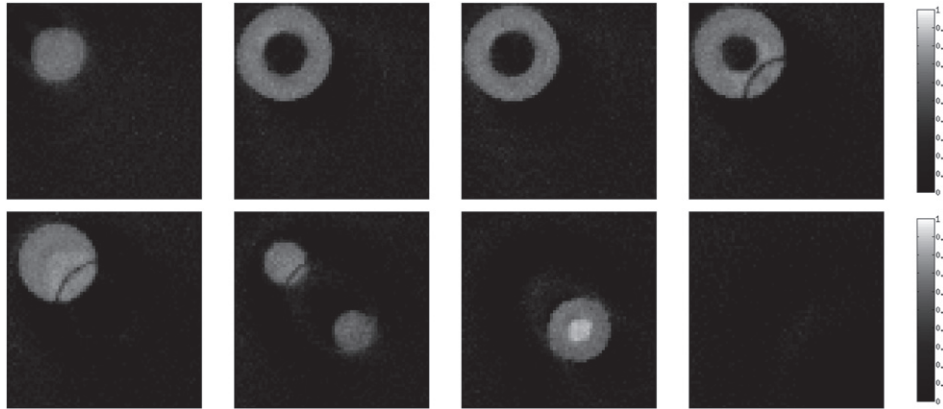
14
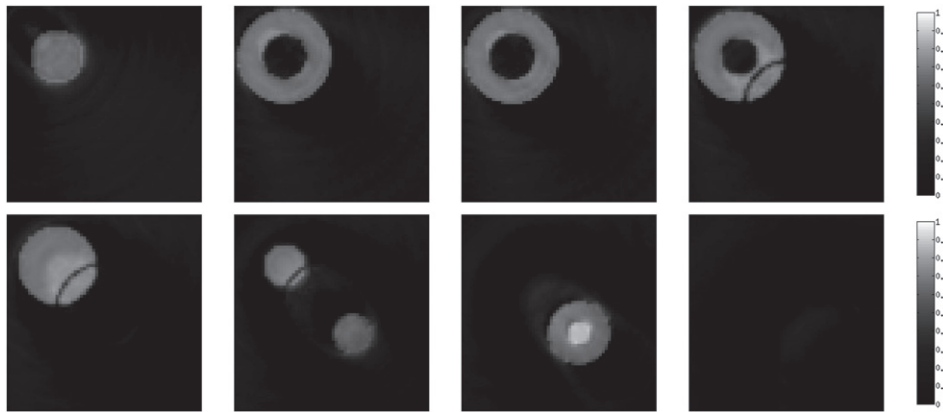
Figure 5. Reconstructions from noiseless data. Errors are NMSE $=$ 0.32%, NMAE $=$ 3.81%. Regularization parameter $\lambda = 0.01$.
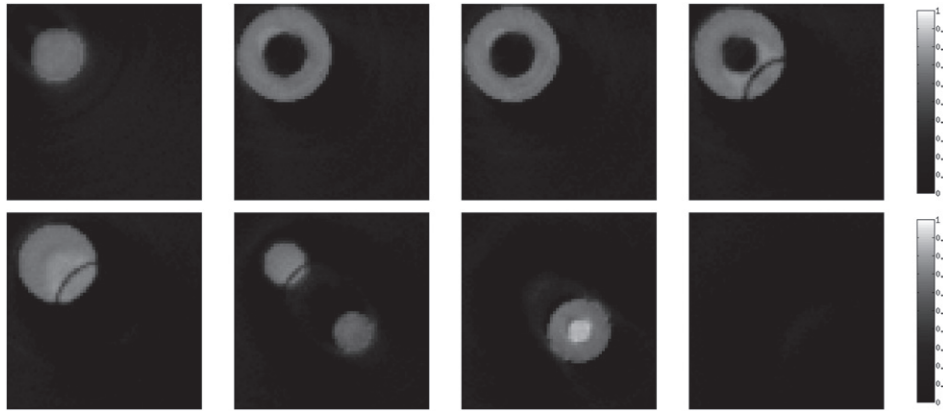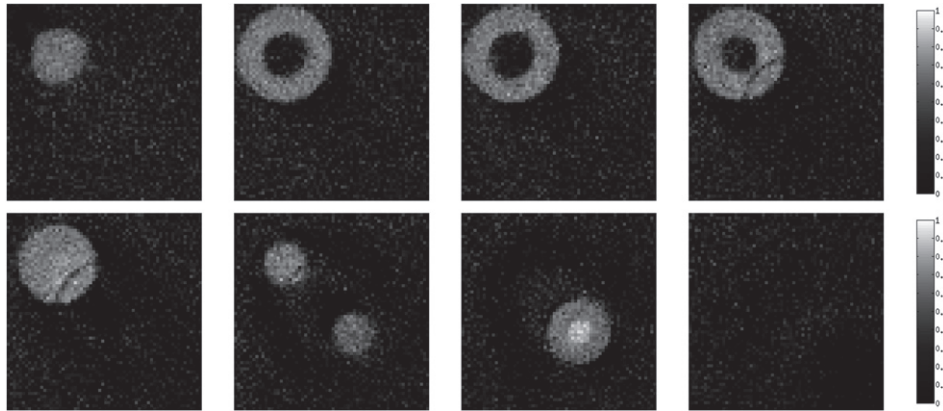

Figure 6. Reconstructions from noisy data with SNR $=$ 30 dB (relative level of noise 3%). Errors are NMSE $=$ 0.34%, NMAE $=$ 3.77%. Regularization parameter $\lambda = 0.05$.

variable step $\Delta \gamma = \cos^{-1}\left(p/R\right)/N_\gamma$, with $N_\gamma = 256$ and $N_\psi = 256$. Figure 4 shows simulated data for different values of angle α. The trapezoidal rule was used to perform numerical integration. According to the discretization chosen for data, the order of the spherical harmonics expansion was $N = 256$ ($N_\alpha = 2N + 1$). In order to get more realistic simulations, data $\mathbf{g} = \mathbf{g}_{nk}^j$ were also corrupted with additive Gaussian noise with zero mean. Noise variance was manually adjusted to get several signal-to-noise ratios: SNR $=$ 10, 20 and 30 dB. These SNR correspond to $\epsilon = 29$, 10 and 3% noise levels where $\epsilon = 100\|\tilde{\mathbf{g}} - \mathbf{g}\|_2/\|\mathbf{g}\|_2$, and $\tilde{\mathbf{g}}$ is the corrupted data. In order to asses the quality of reconstruction we used the following measures of error: the normalized mean square error (%)

$$\text{NMSE} = \frac{100}{N^3} \frac{\|\mathbf{f} - \tilde{\mathbf{f}}\|_2^2}{\max_i \left\{\mathbf{f}_i^2\right\}}, \tag{37}$$

Figure 7. Reconstructions from noisy data with SNR = 20 dB (relative level of noise 10%). Errors are NMSE = 0.40%, NMAE = 4.35%. Regularization parameter $\lambda = 0.05$.

Figure 8. Reconstructions from noisy data with SNR = 10 dB (relative level of noise 29%). Errors are NMSE = 0.92%, NMAE = 7.38%. Regularization parameter $\lambda = 0.05$.

and the normalized mean absolute error (%)

$$\text{NMAE} = \frac{100}{N^3} \frac{\|\mathbf{f} - \tilde{\mathbf{f}}\|_1}{\max_i \{\mathbf{f}_i\}}, \tag{38}$$

where $\mathbf{f}$ is the original image and $\tilde{\mathbf{f}}$ is the reconstruction. We used the algorithm in table 1 to carry out reconstructions for two values of the regularization parameter, $\lambda = 0.01$ (noiseless data) and $\lambda = 0.05$ (noisy). These values were chosen heuristically and are the same for all equations in a set (36), i.e. they do not depend on l, m. Figure 5 shows reconstructions for noiseless data and figures 6–8 show reconstructions from corrupted data. No post-processing was applied to images. The original function as well as reconstructions are shown at planes $z = 4, 14, 15, 22, 26, 31, 38$ and 58 from top to bottom and from left to right and error metrics are displayed in figure captions. Reconstructions exhibit acceptable quality: structures inside the object are

distinguished, shapes are kept and error metrics seem to be reasonable. Moreover, the crack is visible in all the images where its is expected. There are, however, background artifacts and blurring, particularly in upper planes. As expected, stronger regularization is required for noisy data and error metrics get worse with the level of noise. Although Tikhonov regularization performs well, reconstructions can be improved using several strategies. Artifacts produced by Gibbs oscillations can be alleviated through an appropriate windowing [28] of the function before step 4 in the algorithm in table 1. Moreover, windows in [28] may be tailored to obtain improved result. Regarding more advanced regularization approaches, the optimal value for the regularization parameter λ can be chosen using the L-curve criterion [29]. There are also algorithms enforcing total variation minimization in the Cartesian domain [30, 31] that can be applied after step 5 in the algorithm in table 1.

5. Discussion

Here, we briefly discuss some details of our approach as well as new perspectives of the work.

The toric transform we study exhibits rotational invariance and we employed spherical harmonic expansion to address the problem of invertibility. In order to study solution uniqueness, we used a theory for Abel and first kind Volterra equations with kernels having zeros on the diagonal [32]. The proof relied on the analysis of the kernel gradient on its diagonal. In other studies on 3D CST [19], spherical harmonic expansion was used together with an approach to solve weakly singular Volterra equations of the first kind based on the theory in [33].

Numerical simulations confirm an additional advantage of this modality: the scanning is feasible when the system is smaller than the object under study. In the proposed simulation we use an object whose side was eight times larger than the radius of the detection sphere.

Since the model neglects attenuation, extra analysis should be carried out when addressing the realistic scenario. When attenuation is significantly low, few photon counts are expected leading to a sparse signal. In such case, the algorithm may be adapted to deal with sparse data. The influence of attenuation is modeled through weighted Radon transforms on tori leading to weighted kernels. Under some assumptions, this mathematical framework may be applied with weighted kernels both in the theoretical treatment as well as in reconstructions. Other works address the reconstruction problem when attenuation is present [18, 34].

From an algorithmic point of view, the reconstruction approach allows to split up the 3D problem in several 1D equations reducing the size of the matrices involved with respect to a standard algebraic treatment. This reduces memory requirements, leads to faster reconstructions and enables higher resolution imaging. Moreover, computation time may be saved through parallelization since the resulting 1D algebraic equations are independent. In addition, the algorithm does not require advanced numerical libraries for handling sparse matrices or implementing regularization. The most complex algorithm in our processing pipeline is the DFT/FFT routine used in the DSHT algorithm. Inverse matrices and Legendre polynomials can be preallocated in memory to accelerate implementation.

6. Conclusion

We studied a Compton scattering tomography in three dimensions suitable for scanning large objects. This system has interesting advantages such as fixed and unique source and compactness. Measured data was modeled by a toric Radon transform. We demonstrated the invertibility of the toric transform by proving the uniqueness of the solutions of the one-dimensional Abel's type equation resulting from its spherical harmonics expansion. In

addition, we developed a reconstruction method based on the discrete spherical harmonics expansion and Tikhonov regularization. Numerical simulations confirm the feasibility of the approach. Future challenges emerge such as incorporating attenuation to the model and dealing with sparse data. Some studies on that direction are on the way.

Acknowledgments

Data availability statement

No new data were created or analysed in this study.

Appendix A. Spherical harmonics expansion

Here, we present the proof lemma 2.1 explaining how to get form (3) to (7). First, we define some useful rotation properties.

A.1. Rotation properties

Given $h^{-1} = u(\alpha)a(\beta)$ as introduced in (2) we define the rotation operator Λ_h by its action on a function f as:

$$(\Lambda_h f)(r\Theta(\gamma, \psi)) = f\left(rh^{-1}\Theta(\gamma, \psi)\right). \tag{A.1}$$

Applying this linear operator Λ_h to a function expanded as in (5) we have

$$(\Lambda_h f)(r\Theta(\gamma, \psi)) = \sum_{l \in \mathbb{N}} \sum_{|m| \leqslant l} f_{lm}(r)(\Lambda_h Y_l^m)(\gamma, \psi). \tag{A.2}$$

Properties (a)–(C) will be useful in what follows:

(a) Any rotated spherical harmonic of degree l is a linear combination of Y_l^n with $|n| \leqslant l$:

$$(\Lambda_h Y_l^m)(\gamma, \psi) = \sum_{|n| \leqslant l} Y_l^n(\gamma, \psi) D_{n,m}^{(l)}(h). \tag{A.3}$$

(b) Matrices $D^{(l)}(h)$ verify:

$$D_{0,m}^{(l)}(h) = \overline{D_{m,0}^{(l)}}(h^{-1}). \tag{A.4}$$

(c) From the definition of the matrix entries $D_{n,m}^{(l)}(h)$ [22], it follows that:

$$Y_l^m(\alpha, \beta) = \sqrt{\frac{2l+1}{4\pi}} \overline{D_{m,0}^{(l)}}(h^{-1}). \tag{A.5}$$

See [20, 22] for details.

A.2. Proof of lemma 2.1

Proof.   From (3) and (A.1) we have:

$$\mathcal{R}_{\mathcal{T}}f(\alpha,\beta,\omega) = \int_0^{2\omega-\pi} \mathrm{d}\gamma \int_0^{2\pi} \mathrm{d}\psi \, r^{\omega}(\gamma) \frac{\sin\gamma}{\sin\omega} \left(\Lambda_h f\right)\left(r^{\omega}(\gamma)\Theta(\gamma,\psi)\right). \quad \text{(A.6)}$$

Using (A.2) and (A.3), we can write:

$$\mathcal{R}_{\mathcal{T}}f(\alpha,\beta,\omega) = \sum_{l\in\mathbb{N}} \sum_{|m|\leqslant l} \int_0^{2\omega-\pi} \mathrm{d}\gamma \int_0^{2\pi} \mathrm{d}\psi \, r^{\omega}(\gamma) \frac{\sin\gamma}{\sin\omega} f_{lm}\left(r^{\omega}(\gamma)\right) \left(\Lambda_h Y_l^m\right)(\gamma,\psi)$$

$$= \sum_{l\in\mathbb{N}} \sum_{|m|\leqslant l} \sum_{|n|\leqslant l} \int_0^{2\omega-\pi} \mathrm{d}\gamma$$

$$\times \int_0^{2\pi} \mathrm{d}\psi \, r^{\omega}(\gamma) \frac{\sin\gamma}{\sin\omega} f_{lm}\left(r^{\omega}(\gamma)\right) Y_l^n(\gamma,\psi) D_{n,m}^{(l)}(h). \quad \text{(A.7)}$$

Now, using (4) and performing the integration on variable ψ, we have that the only non-vanishing term is the $n=0$ term, so:

$$\mathcal{R}_{\mathcal{T}}f(\alpha,\beta,\omega) = \sum_{l\in\mathbb{N}} \sum_{|m|\leqslant l} \sum_{|n|\leqslant l} \int_0^{2\omega-\pi} \mathrm{d}\gamma \int_0^{2\pi} \mathrm{d}\psi \, r^{\omega}(\gamma) \frac{\sin\gamma}{\sin\omega} f_{lm}\left(r^{\omega}(\gamma)\right) (-1)^n$$

$$\times \sqrt{\frac{(2l+1)(l-n)!}{4\pi(l+n)!}} P_l^n(\cos\gamma) \mathrm{e}^{\mathrm{i}n\psi} D_{n,m}^{(l)}(h)$$

$$= \sum_{l\in\mathbb{N}} \sum_{|m|\leqslant l} 2\pi \int_0^{2\omega-\pi} \mathrm{d}\gamma \, r^{\omega}(\gamma) \frac{\sin\gamma}{\sin\omega} f_{lm}\left(r^{\omega}(\gamma)\right)$$

$$\times P_l^0(\cos\gamma) \sqrt{\frac{(2l+1)}{4\pi}} D_{0,m}^{(l)}(h)$$

$$= \sum_{l\in\mathbb{N}} \sum_{|m|\leqslant l} \sqrt{\frac{(2l+1)}{4\pi}} D_{0,m}^{(l)}(h) 2\pi$$

$$\times \int_0^{2\omega-\pi} \mathrm{d}\gamma \, r^{\omega}(\gamma) \frac{\sin\gamma}{\sin\omega} f_{lm}\left(r^{\omega}(\gamma)\right) P_l^0(\cos\gamma).$$

$$\text{(A.8)}$$

Then, using properties (A.4) and (A.5) we arrive to

$$\mathcal{R}_{\mathcal{T}}f(\alpha,\beta,\omega) = \sum_{l\in\mathbb{N}} \sum_{|m|\leqslant l} Y_l^m(\alpha,\beta) \; 2\pi$$

$$\times \int_0^{2\omega-\pi} \mathrm{d}\gamma \, r^{\omega}(\gamma) \frac{\sin\gamma}{\sin\omega} f_{lm}\left(r^{\omega}(\gamma)\right) P_l^0(\cos\gamma). \quad \text{(A.9)}$$

Finally, the factor accompanying the l,m-spherical harmonic is the l,m-coefficient of the Fourier expansion of $(\mathcal{R}_{\mathcal{T}}f)$ in terms of the scattering angle ω and we get (7). This completes the proof.   □

19

Appendix B. Derivation of equation (17)

We use basic algebra for rewriting equation (16) as (17). Splitting up summation ranges in (16), we have

$$
K_l(p,r) = \sum_{n=0}^{3} a_n \sum_{k=0}^{n} \binom{n}{k} Q_3^{n-k} Q_4^k \left[\left((-1)^{n-k} + 1 \right) Q_1 \sqrt{p-r}^{\,n-k} \right.
$$

$$
+ \left((-1)^{n-k} - 1 \right) Q_2 \sqrt{p-r}^{\,n-k+1} \Big]
$$

$$
+ \sum_{n=4}^{l} a_n \left\{ \sum_{k=0}^{n-4} \binom{n}{k} Q_3^{n-k} Q_4^k \left[\left((-1)^{n-k} + 1 \right) Q_1 \sqrt{p-r}^{\,n-k} \right. \right.
$$

$$
+ \left((-1)^{n-k} - 1 \right) Q_2 \sqrt{p-r}^{\,n-k+1} \Big]
$$

$$
+ \sum_{k=n-3}^{n} \binom{n}{k} Q_3^{n-k} Q_4^k \left[\left((-1)^{n-k} + 1 \right) Q_1 \sqrt{p-r}^{\,n-k} \right.
$$

$$
+ \left((-1)^{n-k} - 1 \right) Q_2 \sqrt{p-r}^{\,n-k+1} \Big] \right\}. \tag{B.1}
$$

Now, we evaluate summations at the combinations of indices for which $n - k \leqslant 4$ and $n - k + 1 \leqslant 4$. Then, we group the resulting terms in four summands with factors $(p-r)$, $(p-r)^2$, higher powers of $(p-r)$ and independent terms.

$$
K_l(p,r) = \sum_{n=4}^{l} a_n \sum_{k=0}^{n-4} \binom{n}{k} Q_3^{n-k} Q_4^k \left[\left((-1)^{n-k} + 1 \right) Q_1 \sqrt{p-r}^{\,n-k} \right.
$$

$$
+ \left((-1)^{n-k} - 1 \right) Q_2 \sqrt{p-r}^{\,n-k+1} \Big]
$$

$$
+ (p-r)^2 \left[-2a_3 \binom{3}{0} Q_3^3 Q_2 - 2 \sum_{n=4}^{l} a_n \binom{n}{n-3} Q_3^3 Q_4^{n-3} Q_2 \right]
$$

$$
+ 2(p-r) \left\{ \left[Q_3^2 Q_1 \sum_{n=4}^{l} a_n \binom{n}{n-2} Q_4^{n-2} \right. \right.
$$

$$
- Q_3 Q_2 \sum_{n=4}^{l} a_n \binom{n}{n-1} Q_4^{n-1} \Big]
$$

$$
+ Q_3^2 Q_1 \left[a_2 \binom{2}{0} + a_3 \binom{3}{1} Q_4 \right]
$$

$$
- Q_3 Q_2 \left[a_1 \binom{1}{0} + a_2 \binom{2}{1} Q_4 + a_3 \binom{3}{2} Q_4^2 \right] \right\}
$$

$$
+ 2Q_1 \left[\sum_{n=4}^{l} a_n \binom{n}{n} Q_4^n + a_3 \binom{3}{3} Q_4^3 + a_2 \binom{2}{2} Q_4^2 \right.
$$

$$+ a_1 \begin{pmatrix} 1 \\ 1 \end{pmatrix} Q_4 + a_0 \begin{pmatrix} 0 \\ 0 \end{pmatrix} \Bigg]. \tag{B.2}$$

Finally, writing the last term as a single summation in $n = 0, \ldots, l$ and adjusting indices in the double summation in the first line to absorb the terms containing $(p - r)^2$ we get to (17) as we wanted to show.

$$
K_l(p, r) = 2Q_1 \sum_{n=0}^{l} a_n Q_4^n + 2(p - r)
$$

$$
\times \Bigg[\frac{1}{2} Q_3^2 Q_1 \sum_{n=2}^{l} a_n n(n - 1) Q_4^{n-2} - Q_3 Q_2 \sum_{n=1}^{l} a_n n Q_4^{n-1} \Bigg]
$$

$$
+ \sum_{n=3}^{l} a_n \sum_{k=0}^{n-3} \binom{n}{k} Q_3^{n-k} Q_4^k \left[\left((-1)^{n-k} + 1 \right) Q_1 \sqrt{p - r}^{\,n-k} \right.
$$

$$
+ \left. \left((-1)^{n-k} - 1 \right) Q_2 \sqrt{p - r}^{\,n-k+1} \right]. \tag{B.3}
$$

Appendix C. An algorithm for discrete spherical harmonics expansion

Here, we describe succinctly our implementation of the forward-inverse discrete spherical harmonics transform (DSHT-IDSHT). The technique is based on the algorithms for the discrete Fourier and Legendre transforms as described in [20, 28, 35]. Let us be the discrete function $\mathbf{F}_{kn}^{j} = F(r_j, \theta_k, \varphi_n)$ sampled with the following parameters $\Delta r = (r_{\max} - r_{\min})/(N_r - 1)$ and $\Delta \varphi = 2\pi/(2N + 1)$ with their corresponding indices $j = 0, \ldots, N_r - 1$ and $n = -N, \ldots, N$. Discrete values of variables for radial and azimuthal variables are $r_j = j\Delta r + r_{\min}$ and $\varphi_n = 2\pi n/(2N + 1)$. Latitude variable θ can be arbitrarily sampled in the interval $[0, \pi]$ and is labeled θ_k, $k = 1, \ldots, N_\theta$, we used uniform sampling. The relationship between the discrete function $\mathbf{F}_{kn}^{j}$ and its representation in the domain of discrete spherical harmonics $\mathbf{F}_{lm}^{j}$ is summarized in the diagram:

$$
\mathbf{F}_{nk}^{j} \underset{\text{IDSHT}}{\overset{\text{DSHT}}{\rightleftarrows}} \mathbf{F}_{lm}^{j} \quad : \quad \left\{ \mathbf{F}_{kn}^{j} \right\} \underset{N \cdot \text{IDFT}}{\overset{\frac{1}{N} \cdot \text{DFT}}{\rightleftarrows}} \left\{ \mathbf{F}_{km}^{j} \right\} \underset{\text{DLT}}{\overset{\text{IDLT}}{\rightleftarrows}} \left\{ \mathbf{F}_{lm}^{j} \right\},
$$

while the first block is given by the well known discrete Fourier pairs (DFT-IDFT), the second one is given by the associated discrete Legendre transform pairs (DLT-IDLT)

$$
\mathbf{F}_{km}^{j} = \text{DLT}^m \left\{ \mathbf{F}_{lm}^{j} \right\} = \sum_{l=|m|}^{N} \mathbf{F}_{lm}^{j} q_l^m P_l^m(t_k), \tag{C.1}
$$

and

$$
\mathbf{F}_{lm}^{j} = \text{IDLT}^m \left\{ \mathbf{F}_{km}^{j} \right\} = \sum_{k=1}^{N_\theta} \mathbf{F}_{km}^{j} q_l^m P_l^m(t_k) w_k, \tag{C.2}
$$

where $m = -N, \ldots, N$, $l = |m|, \ldots, N$, $t_k = \cos \theta_k$, w_k are the Gaussian quadrature coefficients and

$$q_l^m = (-1)^m \sqrt{\frac{2l+1}{4\pi} \frac{(l-m)!}{(l+m)!}}. \qquad (C.3)$$

An alternative implementation can be found in [20].

ORCID iDs

J Cebeiro ⓘ https://orcid.org/0000-0003-2070-4016
C Tarpau ⓘ https://orcid.org/0000-0002-8653-9490
M A Morvidone ⓘ https://orcid.org/0000-0002-6338-2830
D Rubio ⓘ https://orcid.org/0000-0001-7180-1401
M K Nguyen ⓘ https://orcid.org/0000-0003-1192-0980

References

[1] Norton S J 1994 Compton scattering tomography *J. Appl. Phys.* **76** 2007–15
[2] Cebeiro J, Nguyen M K, Morvidone M A and Noumowé A 2017 New 'improved' Compton scatter tomography modality for investigative imaging of one-sided large objects *Inverse Probl. Sci. Eng.* **25** 1676–96
[3] Webber J and Miller E L 2020 Compton scattering tomography in translational geometries *Inverse Problems* **36** 025007
[4] Tarpau C, Cebeiro J and Nguyen M K 2019 A new bi-imaging NDT system for simultaneous recovery of attenuation and electronic density maps *11th Int. Conf. Non Destructive Testing Aerospace*
[5] Jones K C, Redler G, Templeton A, Bernard D, Turian J V and Chu J C H 2018 Characterization of Compton-scatter imaging with an analytical simulation method *Phys. Med. Biol.* **63** 025016
[6] Redler G, Jones K C, Templeton A, Bernard D, Turian J and Chu J C H 2018 Compton scatter imaging: a promising modality for image guidance in lung stereotactic body radiation therapy *Med. Phys.* **45** 1233–40
[7] Cormack A M 1981 The Radon transform on a family of curves in the plane *Proc. Am. Math. Soc.* **83** 325
[8] Cormack A M 1982 The Radon transform on a family of curves in the plane. II *Proc. Am. Math. Soc.* **86** 293
[9] Cormack A M 1984 Radon's problem-old and new *SIAM-AMS Proc.* **14** 33–9
[10] Truong T T and Nguyen M K 2011 Radon transforms on generalized Cormack's curves and a new Compton scatter tomography modality *Inverse Problems* **27** 125001
[11] Truong T T and Nguyen M K 2011 On new V-line transforms in R^2 and their inversion *J. Phys. A: Math. Theor.* **44** 13
[12] Truong T T and Nguyen M K 2012 Recent developments on compton scatter tomography: theory and numerical simulations *Numerical Simulation: From Theory to Industry* ed M Andriychuk (Rijeka: INTECH) ch 6 pp 102–28
[13] Webber J 2016 X-ray Compton scattering tomography *Inverse Probl. Sci. Eng.* **24** 1323–46
[14] Norton S J 2019 Compton-scattering tomography with one source and one detector: a simple derivation of the filtered-backprojection solution *Inverse Probl. Sci. Eng.* **28** 894–905
[15] Tarpau C, Cebeiro J, Morvidone M A and Nguyen M K 2020 A new concept of Compton scattering tomography and the development of the corresponding circular radon transform *IEEE Trans. Radiat. Plasma Med. Sci.* **4** 433–40
[16] Webber J W and Quinto E T 2020 Microlocal analysis of a Compton tomography problem *SIAM J. Imag. Sci.* **13** 746–74

[17] Tarpau C, Cebeiro J, Nguyen M K, Rollet G and Morvidone M A 2020 Analytic inversion of a Radon transform on double circular arcs with applications in Compton scattering tomography *IEEE Trans. Comput. Imaging* **6** 958–67

[18] Rigaud G and Hahn B 2018 3D Compton scattering imaging and contour reconstruction for a class of Radon transforms *Inverse Problems* **34** 075004

[19] Webber J W and Lionheart W R B 2018 Three dimensional Compton scattering tomography *Inverse Problems* **34** 084001

[20] Driscoll J R and Healy D M 1994 Computing Fourier transforms and convolutions on the 2-sphere *Adv. Appl. Math.* **15** 202–50

[21] Quinto E T 1983 The invertibility of rotation invariant Radon transforms *J. Math. Anal. Appl.* **91** 510–22

[22] Biedenharn L C and Louck J D 1981 *Angular Momentum in Quantum Physics* (Reading, MA: Addison-Wesley)

[23] Laden H N 1938 An historical and critical development of the theory of Legendre polynomials before 1900 *PhD Thesis* University of Maryland

[24] Schiefeneder D and Haltmeier M 2017 The Radon transform over cones with vertices on the sphere and orthogonal axes *SIAM J. Appl. Math.* **77** 1335–51

[25] Jackson J D 1999 *Classical Electrodynamics* 3rd edn (New York: Wiley)

[26] Haltmeier M, Moon S and Schiefeneder D 2017 Inversion of the attenuated V-line transform with vertices on the circle *IEEE Trans. Comput. Imaging* **3** 853–63

[27] Weiss R and Anderssen R S 1971 A product integration method for a class of singular first kind Volterra equations *Numer. Math.* **18** 442–56

[28] Taguchi K, Zeng G L and Gullberg G T 2001 Cone-beam image reconstruction using spherical harmonics *Phys. Med. Biol.* **46** 127–38

[29] Hansen P 2001 *Computational Inverse Problems in Electrocardiology* ed P Johnston (Southampton: WIT Press) pp 119–42 chap The L-curve and its use in the numerical treatment of inverse problems

[30] Condat L 2013 A direct algorithm for 1D total variation denoising *IEEE Signal Process. Lett.* **20** 1054–7

[31] Condat L 2014 A generic proximal algorithm for convex optimization—application to total variation minimization *IEEE Signal Process. Lett.* **21** 985–9

[32] Moon S and Haltmeier M 2017 Analytic inversion of a conical Radon transform arising in application of Compton cameras on the cylinder *SIAM J. Imag. Sci.* **10** 535–57

[33] Bownds J M 1976 On solving weakly singular Volterra equations of the first kind with Galerkin approximations *Math. Comput.* **30** 747

[34] Rigaud G and Hahn B N 2020 Reconstruction algorithm for 3D Compton scattering imaging with incomplete data *Inverse Probl. Sci. Eng.* 1–23

[35] Basko R, Zeng G L and Gullberg G T 1998 Application of spherical harmonics to image reconstruction for the Compton camera *Phys. Med. Biol.* **43** 887–94